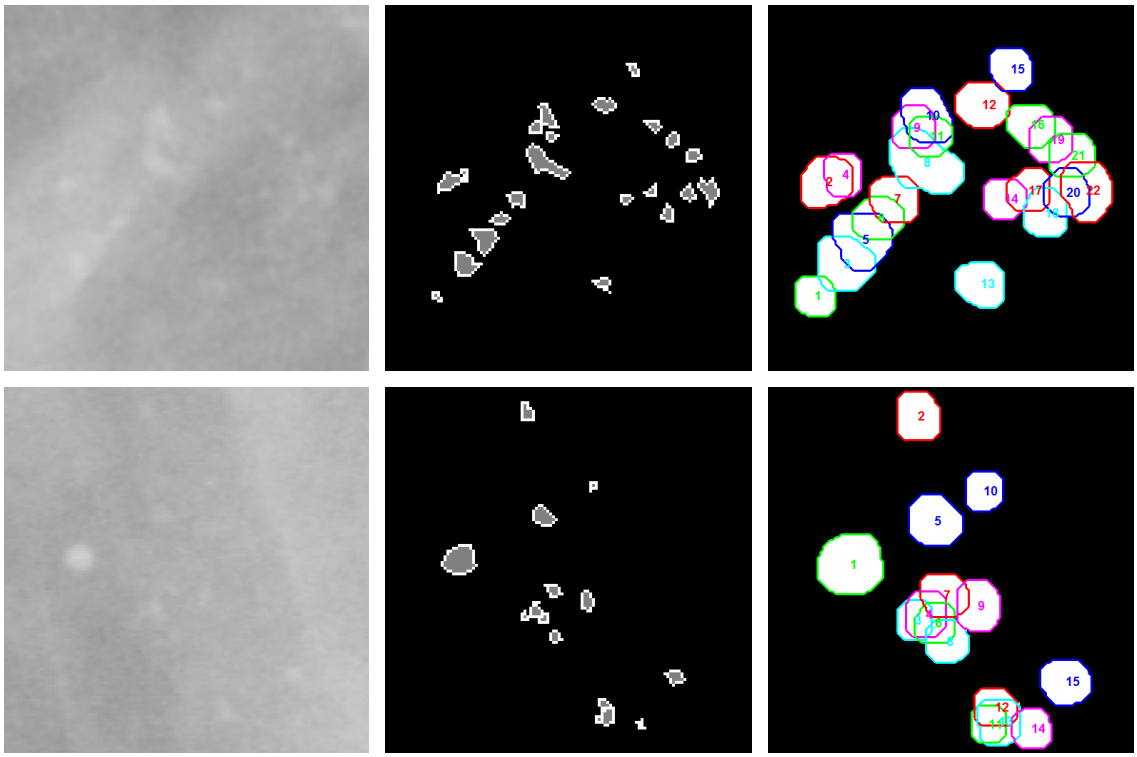

Figure 1: Example microcalcification clusters: malignant (top row) and benign (bottom row). Left column: original image patches; middle column: manually segmented microcalcifications; right column: dilated microcalcifications (at scale 7). Note that microcalcification No. 16 is not displayed in the bottom images as this falls outside the zoomed region.

roughness of individual microcalcifications. Betal *et al*. [1] analysed four shape properties of individual microcalcifications. Chan *et al*. [3] used morphological features to describe the size, shape, and contrast of individual microcalcifications and their variations within the cluster. Cluster features were used in [1, 5, 9] to describe the global properties of the cluster. The greylevel variations and texture features within the region of interest were investigated in [2] and [5]. The performance of different types of features for microcalcification classification was compared in [12], where the multiscale representation based on multiwavelet transform, shape and texture features were investigated.

Malignant microcalcifications tend to be small, numerous and densely distributed, while benign microcalcifications are generally larger, smaller in number and more diffusely distributed [11]. This difference results in various topological structures of microcalcification clusters. The distribution of microcalcifications associated with a malignant process may be different from that associated with a benign process [6]. We investigate the connectivity between individual microcalcifications using morphological operations at multiple scales.

## 2 Data and Method

The data used in this paper are twenty image patches ($512 \times 512$ pixels) taken from the Mammographic Image Analysis Society (MIAS) database [13], each containing a microcalcification cluster. There are nine malignant and eleven benign cases (biopsy proven) in the dataset. All individual microcalcifications have been manually segmented by an expert radiologist. The median number of microcalcifications in the clusters is 27. There are a

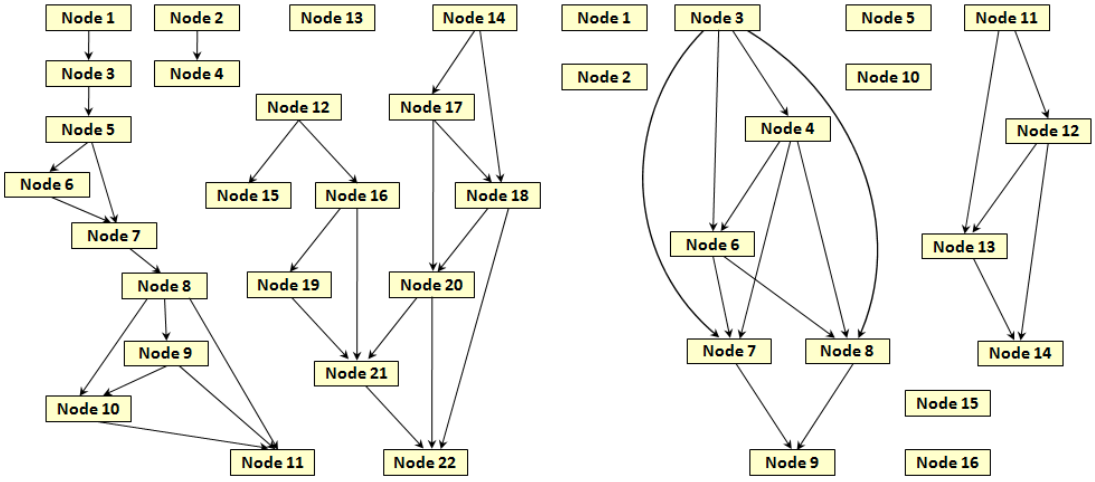


Figure 2: Microcalcification graphs: (a) malignant ($n_s = 4$, $\delta_s = 1.23$); (b) benign ($n_s = 8$, $\delta_s = 1.00$). The numbering of nodes is consistent with the sequence number in Figure 1.

few outliers and 80% of the clusters are within the 6 to 62 range. Figure 1 shows example microcalcification clusters and corresponding manual annotations. In addition, an approach developed by Oliver *et al*. [8] is used to detect microcalcifications. Probability images are obtained where high values indicate microcalcifications. To segment microcalcifications, the probability images are binarised using a threshold determined using ROC analysis.

## 2.1 Morphological Operation

Multiscale morphological dilation is performed on individual microcalcifications using a disk-shaped structuring element with a radius equal to the scale (see the right column of Figure 1, where each individual microcalcification is ordered with a sequence number and the boundaries of dilated microcalcifications are displayed using different colours). It indicates that the morphological dilation adds neighbouring pixels to the boundaries of individual microcalcifications, resulting in changes in the connectivity between individual microcalcifications within clusters.

## 2.2 Microcalcification Graph

The topology of individual microcalcifications within the cluster is represented in graphical form. A microcalcification graph is constructed based on the spatial connectivity relationship between microcalcifications, where each node represents one microcalcification, and two nodes are linked by an edge if the corresponding two microcalcifications are connected or overlap with each other. Here, we generate a directed graph where the nodes are ordered according to the spatial location of the corresponding microcalcifications in the image patch, and two connected nodes are linked by a directed edge from the smaller to the larger numbered node. The resulting graphs of dilated microcalcifications in Figure 1 are shown in Figure 2. We focus on two properties of the microcalcification graph. The first property is the number of independent subgraphs within the graph, which represents the number of independent connected components within the microcalcification cluster. The second property is the degree of each node defined as the number of edges starting from the node, which describes the connectivity of the corresponding microcalcification with its neighbours.

We define an upper-triangular adjacency matrix to encode the directed microcalcification graph, denoted by $A = (a_{ij})$, $a_{ij} \in \{0,1\}$, $i,j = 1,\ldots,m$, where $m$ is the number of nodes within the graph. Node $i$ and node $j$ are connected if $a_{ij} = 1$. Node $i$ is the source node and node $j$ is the sink node. A source node $i$ is called a *root* node if $\sum_{k=1}^{m} a_{ki} = 0$. A sink node $j$ is called a *terminal* node if $\sum_{k=1}^{m} a_{jk} = 0$. A *path* from node $i$ to node $j$ is defined as a sequence of nodes starting from node $i$ and ending with node $j$. The number of independent subgraphs (denoted by $n$) is determined by traversing the graph. We traverse the graph starting at each *root* node and explore as far as possible along each *path* until arriving at the *terminal* node. The traversal sequences including common nodes are combined into a single sequence. The number of the final sequences is the number of independent subgraphs. The degree of node $i$ (denoted by $\delta(i)$) is computed by $\delta(i) = \sum_{k=1}^{m} a_{ik}$.

### 2.3 Multiscale Topological Feature Vector

We generate a set of microcalcification graphs $G = (G_0, G_1, \ldots, G_{S-1})$ based on dilated microcalcifications at $S$ scales. We extract properties from $G$ and form two feature vectors $N = (n_0, n_1, \ldots, n_{S-1})$ and $\Delta = (\delta_1, \delta_2, \ldots, \delta_{S-1})$, where $n_s (s = 0,1,\ldots,S-1)$ is the number of independent subgraphs at scale $s$, and $\delta_s (s = 0,1,\ldots,S-1)$ is the average degree of nodes at scale $s$, computed by $\frac{1}{m}\sum_{i=1}^{m} \delta(i)_s$. We normalise $N$ and $\Delta$ by $n_s/m$ and $\delta_s / \max \delta(i)_s$, where $\max \delta(i)_s$ is the maximum degree of nodes at scale $s$. Finally, the two normalised vectors are concatenated into a single feature vector, which can be used for the classification of malignant and benign microcalcification clusters.

## 3 Experimental Results

For each microcalcification cluster, we analysed the morphological topology of microcalcifications at 129 scales ($s = 0,1,\ldots,128, S = 129$). As described in Section 2, we computed $n_s$ and $\delta_s$ using the corresponding microcalcification graph at scale $s$. The dimensionality of the obtained multiscale topological feature vectors was 258.

A k-nearest neighbour (kNN) classifier and a leave-one-out methodology were used for classification. The Euclidean distance was used to measure the similarity between feature vectors. The sequential forward selection (SFS) algorithm was applied to select the most discriminating features. In the feature selection process, SFS was performed based on the training set excluding the testing sample to avoid bias. For different training sets, on average approximate 90 features were retained for the feature set (manual data) extracted from the manual annotations and approximate 120 features were retained for the feature set (CAD data) extracted from the automatic detections. The most frequently selected features (occurrence $> 80\%$) are mainly within the scale range of $[1,32]$ for the manual data and $[28,68]$ for the CAD data. For the manual data, using the unreduced feature space, the best classification accuracy (CA) was 90% for $k = 3$, where nine of the eleven benign cases were classified correctly without misclassifying any malignant cases. Using the reduced feature space, the best CA was increased to 95% with one benign case misclassified. For the CAD data, using the unreduced feature space, the best CA was 85% for $k = 5$ with two benign and one malignant cases misclassified. Using the reduced feature space, the best CA was 95% for $k = 3$ with one malignant case misclassified. This indicates the method is robust with regard to microcalcification segmentation and performs well on the CAD detection results.

Table 1: Comparison of our achieved results with those obtained by some related work.

| Method | Database | # Case | Feature | Classifier | Result |
|---|---|---|---|---|---|
| [10] | unknown | 18 | shape | kNN | $CA = 100\%$ |
| [1] | Liverpool | 38 | shape/cluster | kNN | $A_z = 0.79 A_z = 0.84$ |
| [7] | DDSM | 183 | shape | $\alpha_{max}$ | $A_z = 0.96$ |
| [3] | unknown | 145 | morphological | LDC | $A_z = 0.79$ |
| [5] | unknown | 191 | texture & cluster | ANN | $A_z = 0.86$ |
| [9] | MIAS | 25 | cluster | SVM | $A_z = 0.81$ |
| [2] | unknown | 54 | texture | ANN | $A_z = 0.88$ |
| [12] | Nijmegen | 103 | multiwavelet | kNN | $A_z = 0.89$ |
| Our | MIAS (manual) | 20 | multiscale topology | kNN | $CA = 95\%$ $A_z = 0.93$ |
| | MIAS (CAD) | 20 | multiscale topology | kNN | $CA = 95\%$ $A_z = 0.92$ |

To quantitatively assess the classification performance of the multiscale topological features, a ROC curve was constructed. The ROC curve represents the trade-off between the true positive rate (TPR) against the false positive rate (FPR). The construction of the ROC curve is based on a decision criterion which can be regarded as a threshold to decide a test sample as either positive or negative. We defined a malignancy measure (denoted by $M$) as the decision criterion based on the kNN classifier. The malignancy measure $M$ of a testing microcalcification cluster was defined to be the number of malignant clusters among its $k$ nearest neighbours, ranging from 0 to $k$. Thus, a threshold $L$ was set from -1 to $k$, and the testing cluster was classified as malignant if $M$ was larger than $L$. When $L = -1$, all the microcalcification clusters were classified as malignant with TPR and FPR equal to 1. At the other extreme, when $L = k$, all the microcalcification clusters were classified as benign with TPR and FPR equal to 0. The remaining TPR and FPR were obtained by varying $L$ from 0 to $k-1$. This produced $k+2$ points of TPR and FPR. Finally, the area under the ROC curve (denoted by $A_z$) was computed using the trapezoidal rule. We tested three $k$ values: $k = 3$, $k = 5$, and $k = 7$. For the manual data, the obtained $A_z$ was 0.88, 0.91, 0.85, and 0.91, 0.93, 0.87, using the unreduced and reduced feature space, respectively. For the CAD data, the obtained $A_z$ was 0.81, 0.88, 0.80, and 0.88, 0.92, 0.86, using the unreduced and reduced feature space, respectively.

We compared our proposed method with some related publications. Table 1 shows a summary of the comparison. It is shown that our method provides comparative results for both manual and CAD segmentation. Note that the various approaches use different images taken from different databases, and therefore it is a qualitative comparison.

# 4 Conclusions

This is a novel approach to investigate the morphological topology and connectivity of microcalcifications for discriminating malignant from benign clusters. Unlike most features in previous publications extracted at a single scale, a representation covering the multiscale characteristics was developed in this paper. To evaluate the validity of this method, we used manually segmented microcalcifications and CAD detection results. Good classification results were obtained for both types of data. This indicates the robustness of this method to detection errors and the potential application in CAD systems. As feature work, alternative

approaches to feature selection (e.g. genetic algorithm) and other classifiers (e.g. decision tree, artificial neural network, and support vector machine) will be employed for classification. The definition of a similarity measure between graphs will be further investigated in order to realise classification using the graph based representation directly without generating feature vectors. In addition, further evaluation using a larger dataset taken from the DDSM database and a dataset of full-field digital mammograms is ongoing.

# References

[1] D. Betal et al. Segmentation and numerical analysis of microcalcifications on mammograms using mathematical morphology. *British Journal of Radiology*, 70(837):903–917, 1997.

[2] H. P. Chan et al. Computerized classification of malignant and benign microcalcifications on mammograms: Texture analysis using an artificial neural network. *Physics in Medicine and Biology*, 42:549–567, 1997.

[3] H. P. Chan et al. Computerized analysis of mammographic microcalcifications in morphological and texture feature spaces. *Medical Physics*, 25(10):2007–2019, 1998.

[4] H. D. Cheng et al. Computer-aided detection and classification of microcalcifications in mammograms: A survey. *Pattern Recognition*, 36(12):2967–2991, 2003.

[5] A. P. Dhawan et al. Analysis of mammographic microcalcifications using gray-level image structure features. *IEEE TMI*, 15(3):246–259, 1996.

[6] S. A. Feig et al. Evaluation of breast microcalcifications by means of optically magnified tissue specimen radiographs. *Recent Results in Cancer Research*, 105:111–123, 1987.

[7] Y. Ma et al. A novel shape feature to classify microcalcifications. In *Proc. ICIP*, pages 2265–2268, 2010.

[8] A. Oliver et al. Automatic microcalcification and cluster detection for digital and digitised mammograms. *Knowledge-Based Systems*, 28:68–75, 2012.

[9] A. Papadopoulos et al. Characterization of clustered microcalcifications in digitized mammograms using neural networks and support vector machines. *Artificial Intelligence in Medicine*, 34(2):141–150, 2005.

[10] L. Shen et al. Application of shape analysis to mammographic calcifications. *IEEE TMI*, 13(2):263–274, 1994.

[11] E. A. Sickles. Breast calcifications: Mammographic evaluation. *Radiology*, 160(2): 289–293, 1986.

[12] H. Soltanian-Zadeh et al. Comparison of multiwavelet, wavelet, Haralick, and shape features for microcalcification classification in mammograms. *Pattern Recognition*, 37 (10):1973–1986, 2004.

[13] J. Suckling et al. The Mammographic Image Analysis Society digital mammogram database. In *International Congress Series 1069*, pages 375–378, 1994.